Non-Galvanic Mass Transport in Molten Fluoride Salt Isothermal Corrosion Cells

*Cody Falconer¹, William H. Doniger¹, Louis Bailly-Salins², Evan Buxton², Mohamed

Elbakhshwan², Kumar Sridharan^{1,2}, Adrien Couet^{1,2}

²Department of Engineering Physics, University of Wisconsin-Madison, Madison, WI, USA

¹Department of Materials Science & Engineering, University of Wisconsin-Madison, Madison, WI,

Abstract: Mass transport of corrosion products between Ni-201 test samples and 316L capsules in a 500-

hour FLiNaK corrosion experiment has been investigated. In one experiment, the capsule and samples

were electrically connected for galvanic coupling, while in the other they were electrically isolated using

boron-nitride. Post-corrosion characterization of Ni-201 from the two experiments did not reveal any

remarkable differences. Substantial transport of Fe and Cr from the 316L to the Ni-201 via the salt was

observed, with notable diffusion of these elements in the near-surface regions of the Ni-201 samples, while

a Cr-rich film was also observed on their surfaces.

Keywords: mass transport, molten salts, nickel, stainless steel, galvanic corrosion

Introduction

The molten fluoride salt-cooled reactor concept is emerging as a leading candidate for the next

generation of nuclear reactors world-wide, with strong interest being demonstrated by the private sector,

research institutions, and governmental agencies. Corrosion continues to be a challenge for structural

materials in high temperature molten fluoride salts [1-3]. Many recent corrosion studies of candidate

structural alloys have been performed using static isothermal salt capsules with dissimilar materials being

exposed to the salt simultaneously. Here, understanding potential interaction mechanisms between the

corrosion test coupons and the capsule material (i.e. dissimilar materials effect) is critical to accurately

evaluate the performance of the structural alloys in the molten salt environment.

One of the effects of having dissimilar materials in the vicinity of each other in a molten salt medium

is galvanic coupling, wherein the dissimilar materials are placed in electrical contact while submerged in

an electrolyte. Due to differences in corrosion potentials of the materials, the less noble material will corrode

preferentially with respect to the more noble material [4].

Olson et al. and Kondo et al. demonstrated the dramatic effect of dissimilar materials on corrosion rates in static isothermal salt corrosion experiments in high temperature molten LiF-NaF-KF (FLiNaK) when a galvanic couple is established [5, 6]. To eliminate the galvanic couple in high temperature static corrosion testing many studies have utilized a similar corrosion cell as the one described by Olson et al [5] and modified their designs so that the samples are suspended from an electrically insulating ceramic strip [7-12]. However, at the time it was unclear whether or not the dissimilar material effect was strictly due to galvanic coupling or due to an activity gradient mass transport process described by Ozeryanaya [13]. For instance, when GH3535 (a version of Hastelloy-N) samples were tested in a graphite capsule, Ai et al. [14] still observed the formation of a chromium carbide film on the surface of the capsule even when the test samples were electrically isolated from the graphite capsule. From these studies, it appears that electrical insulation does not eliminate all the possible dissimilar material corrosion effects in a metal-graphite system.

Recently, Sun et al. studied the effects that dissimilar alloys have on one another by exposing 316L stainless steel (referred to henceforth as 316L) and Hastelloy-N to FLiNaK in the same graphite corrosion capsule [15]. The samples were kept electrically insulated from the container, but the 316L and Hastelloy-N were placed in direct electrical contact so that a galvanic couple was formed between the two alloys. It was observed that when galvanically connected, the corrosion of 316L was accelerated (higher mass loss) and Hastelloy-N gained mass due to mass transport of Fe from 316L. The authors attributed the mass transport to being purely driven by a galvanic effect through redox reactions since the samples were electrically connected [15].

The present study represents a separate effects experiment, investigating the influence of electrical contact, or galvanic coupling, on dissimilar material corrosion in molten FLiNaK salt at 700 °C. The sample coupon material and the corrosion capsule material were purposefully chosen to differ in their nobilities based on their thermodynamic free energy of formation of their respective fluorides. Ni-201 is relatively stable in molten FLiNaK salt due to the relatively high (less negative) Gibbs free energy of formation of nickel fluoride [16]. Conversely, 316L is relatively active in FLiNaK salt because it contains chromium and

iron which have relatively low Gibbs free energies of formation for their respective fluoride compounds [5, 17]. To facilitate characterization, the corrosion cell consisted of Ni-201 test coupons and a 316L capsule, with the hypothesis that mass transport of the corrosion products would occur based on the differences in Gibbs free energy of fluoride formation of the elements constituting the capsule and the test sample.

2 Experimental Methods

2.1 FLiNaK Salt

FLiNaK (eutectic composition of 46.5% LiF, 11.5% NaF, and 42% KF, in mol.%) was pre-mixed and melted by Materion Corporation for this study. The FLiNaK mixture was prepared using LiF, NaF, and KF powders that were at least 99.9% pure. The powders were mixed and melted in a graphite crucible.

The corrosion experiment was conducted in an ultra-high purity argon atmosphere glovebox where oxygen concentrations and moisture concentrations were maintained below 5 ppm and 1 ppm, respectively. The as-received salt samples were analyzed for trace impurities using inductively coupled plasma - mass spectroscopy (ICP-MS). The ten most prominent impurity elements detected in the salt are listed in Table 1. The salt contained low concentrations of all trace metals except for sulfur which was present at levels of 362 ± 41 ppm. Increased sulfur concentrations, in the form of sulphates, have been shown to increase the corrosion rate of both 316 and a Ni-based alloy in molten FLiNaK [11, 18], but would not affect the basic mass transport mechanisms being investigated in this study.

Table 1: Trace element impurity concentrations in the FLiNaK salt as measured by the ICP-MS

technique.				
Element	Concentration			
	(µg/g)			
S	362 ± 41			
Rb	48 ± 2.5			
Ca	25 ± 3.8			
Р	20 ± 2			
Fe	15 ± 0.8			
В	9.0 ±0.6			
Al	5.8 ± 0.5			
Ni	5.0 ± 0.3			
La	4.3 ± 0.5			
Cr	3.9 ± 0.2			

2.2 Samples and Corrosion Capsule Preparation

Corrosion samples were produced from commercially pure Ni-201 round bar stock from Corrosion Materials, and the nominal composition is reported in Table 2. Several 19 mm x 9.9 mm x 1.7 mm rectangular samples were sectioned from this bar stock, and two 1.6 mm diameter holes were drilled at the top and bottom of each sample to suspend them in the molten salt with Ni wire. The samples were ground to a 1200 grit surface finish using SiC abrasive paper following which they were ultrasonically cleaned with deionized water and acetone The dimensions and the masses of the samples were accurately measured before they were introduced into the salt in the capsule inside the glove box. A set of three samples was used for each test.

Table 2: Nominal composition of the Ni-201 corrosion test samples used in this study.

Element	Ni	Fe	Cr	Co	Cu	С	Mg	Mn	Si	S	Ti
Mass %	99.74	0.007	N/A	0.005	0.011	0.016	0.008	0.16	0.02	0.001	0.002

Corrosion capsules were prepared from 316L tubing 127 mm in length with a 25.4 mm outer diameter and 2.1 mm in wall thickness. A model of the corrosion capsules showing the placement of the test samples is shown in Figure 1. To close one end of the tube, a plug was machined from 316L round stock and welded onto the tube using gas tungsten arc welding (GTAW) by the Edison Welding Institute. The tubes were backfilled with Ar during the welding process to limit oxide formation during welding. The tubes were then polished on the inside and outside to remove any trace oxides from the welding process. The capsules were sonicated in a mixture of Oakite 33 and deionized water overnight to further remove any residual oxides from the welding process.

For one experiment, loose fitting caps were machined from 316L round stock for the capsules such that an electrical contact existed between the Ni-201 samples and the 316L capsule. For the second experiment, the Ni-201 samples and the 316L capsule were electrically isolated with an insulating boron nitride (BN) cap. A hole was drilled through the caps to suspend the samples with 99.5% pure nickel wire.

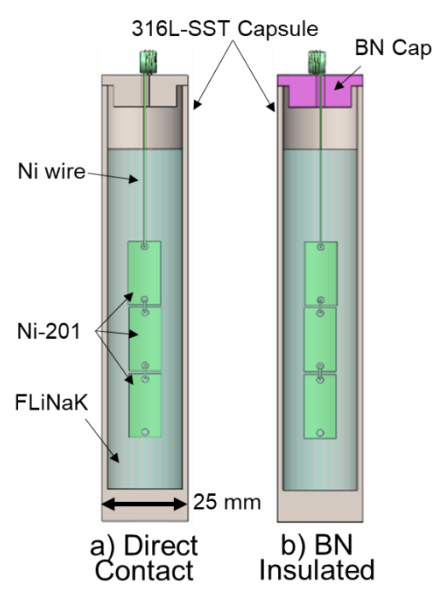


Figure 1: Schematic illustration of 316L corrosion test capsules and Ni-201 test samples suspended with Ni wires. (a) corrosion cell with electrical contact between the samples and the capsule and (b) corrosion cell without electrical contact between the samples and the capsule.

2.3 Experimental System for Corrosion Experiments

Salt preparation was performed inside an ultra-high purity argon environment glovebox. Each 316L corrosion capsule was filled with 70 grams of FLiNaK salt. The volume of salt was calculated assuming the FLiNaK density correlation in Eq. (1) [19], where T is the temperature in Celsius.

$$\rho(T) = 2.530 - 0.00073T [g/cm^3]$$
 Eq. (1)

Using this correlation, the ratio of exposed-metal surface area to volume of salt was calculated to be approximately 2 cm⁻¹ and 0.4 cm⁻¹ for the 316L corrosion capsule and the set of three Ni-201 samples, respectively. The salt was then melted in the capsules at 700 °C using a furnace designed to be inside the glovebox. The samples were introduced into the molten salt at test temperature following which the 316L and BN caps were secured for the two experiments outlined earlier. The samples were then exposed continuously at 700 °C for 500 hours.

After the molten salt exposures, Ni-201 sample sets from both experiments were removed from the salt while the molten salt was still at temperature and allowed to cool in high purity argon. The post corrosion salts from the two experiments were collected by pouring the salt into a 304 stainless steel cup

and the solidification of the salt occurred in less than 5 minutes ensuring that no significant additional corrosion products were introduced in the post-corrosion salt sample.

The samples were cleaned to remove the salt by sonicating in 1 molar Al(NO₃)₃ followed by ultrasonic cleaning in deionized water and acetone. Sample masses were then measured using an electronic balance with 0.002 mg accuracy. The top sample from each sample chain was used for post-corrosion x-ray diffraction (XRD), as well as SEM/EDS analysis of the corrosion surface. XRD characterization was performed on a Panalytical Empyrean using CuK-α x-rays and SEM/EDS was performed on a Zeiss LEO 1530 equipped with an energy dispersive x-ray spectrometer and Pathfinder software. For cross-sectional analysis, the samples were electroplated with Cu in a Cu-sulphate bath, for edge retention during subsequent metallography steps. Salt samples were analyzed at the Wisconsin State Laboratory of Hygiene using ICP-MS. The FLiNaK samples were digested using a mixture of nitric and hydrochloric acid in a microwave-aided Teflon Bomb.

The middle sample was used for glow discharge optical emission spectroscopy (GDOES, Horiba GD Profiler 2) using a pressure of 550 Pa and a power of 40 W for the plasma generation. GDOES was calibrated using sputtering rate correction with five Ni-based alloys of known compositions. The calibration samples covered concentration ranges of 60-100 wt%, 0-25 wt%, 0-5 wt% for Ni, Cr, and Fe respectively. Certified reference materials (low and high alloy steels) were used to build a calibration curve for the quantification of carbon concentration between 0-2 wt% and to extend the concentration range for accurate Ni and Fe quantification.

3 Results

The elements considered most important for the current study were Ni, Fe, and Cr. The ICP-MS compositional analysis of as-received FLiNaK and after corrosion tests from the two experiments are listed in Table 3.

Salts from the tests where the samples were insulated from the 316L corrosion capsule showed slight change in Fe concentration and Ni concentration, an affect that could be attributed to sampling statistics.

For salts from tests where the samples were in electrical contact with the 316L corrosion capsule both Ni and Fe concentrations decreased post-corrosion. In both sample sets, the concentration of Cr increased quite dramatically to similar values of just above 300 wt·ppm. Thus, it appears that the primary source of corrosion products in the post-corrosion salts is from the corrosion of the 316L corrosion capsules as the Ni-201 samples contain negligible Fe and Cr.

Table 3: ICP-MS results from the as-received FLiNaK salt and the post-corrosion salt. Units reported are in $\mu g/g$ (wt:ppm)

are in µg/g (wt ppin)				
Sample	Ni	Fe	Cr	
As-Received FLiNaK	5.0 ± 0.3	15 ± 0.8	3.9 ± 0.2	
BN Insulated	11 ± 1	18 ± 0.8	307 ±32	
Direct Contact	0.5 ± 0.08	4 ± 0.3	306 ± 45	

Ni-201 samples from both experiments exhibited an increase in mass as shown in Figure 2, after exposure to the FLiNaK salt. The BN-insulated sample set showed an average mass gain of 1.26 ± 0.06 mg/cm² whereas the averaged mass gain of the direct electrical contact sample set was 1.12 ± 0.04 mg/cm². The weight gain experienced by both Ni-201 samples sets is attributed to mass transport of corrosion products from the 316L corrosion capsule and deposition on to the surface of Ni-201 samples.

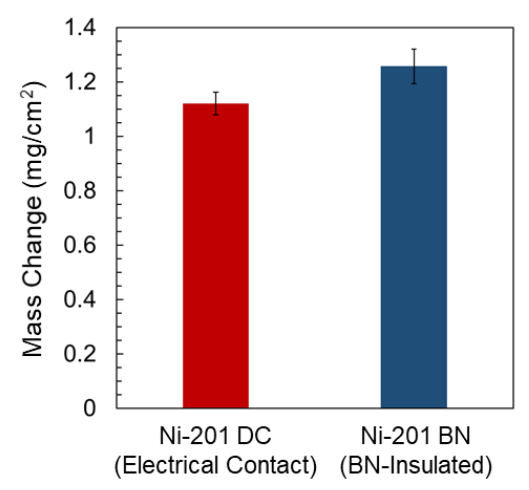


Figure 2: Mass change results after exposure to FLiNaK salt at 700 °C for 500 hours.

XRD analysis was used to identify the formation of any new phase(s) in the near-surface regions of the Ni-201 sample during the corrosion test. In Figure 3A, possible minor peaks at low 2θ theta values could represent a Cr₇C₂₃ (PDF #00-036-1482) phase. This carbide phase is likely a result of corrosion

product transport from the 316L capsule and the presence of carbon in the Materion FLiNaK which were originally prepared in the graphite crucibles. Unfortunately, ICP-MS is not able to determine carbon concentration in the salt so carbon concentration in the as-received FLiNaK could not be verified.

Additionally, Figure 3A shows that there are two ordered FCC phases now present in the near-surface region of the samples. At low 2θ values, better viewed in Figure 3B, the (111) and (200) FCC peaks post-corrosion have shifted to slightly lower 2θ values compared to the peaks in the Ni reference patterns. Additionally, the (111) and (200) peaks in the post-corrosion samples contain a slight shoulder that better matches the (111) and (200) peaks in the Ni reference. The FCC (220), (311), and (222) peaks show separation into two peaks labeled Ni FCC and Ni-Fe-Cr FCC in Figure 3A. The Nelson-Riley function was used to calculate the lattice parameter of both FCC phases present. Using the Ni FCC peaks in the post-corrosion samples the lattice parameter was calculated to be 3.52 Å for both the direct contact and BN-insulated samples which is slightly below the lattice parameter calculated for the Ni reference (a = 3.53 Å).

The shift of the (111) and (200) peaks to lower 2θ values as well as the separation of the (220), (311), and (222) peaks is likely a result of diffusion of Fe and Cr corrosion products, which result in a slight expansion of the Ni-201 lattice parameter in the near surface region. Nelson-Riley analysis of the slightly shifted peaks showed that the lattice parameter of the near-surface regions of the samples to be 3.54 Å and 3.55 Å for the BN-insulated and direct electrical contact samples, respectively.

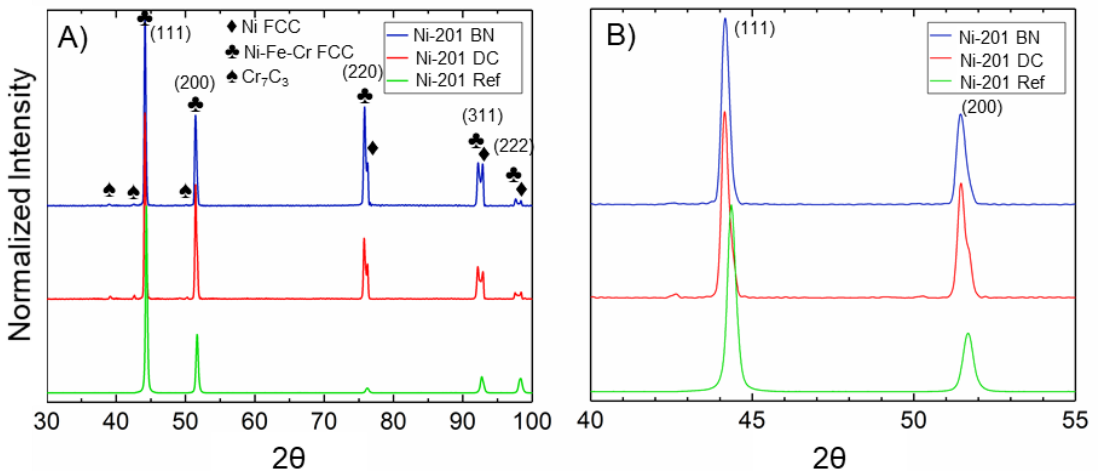


Figure 3: XRD patterns for Ni-201 test samples pre- and post-corrosion. A) full XRD spectrum, B) zoomed in window on the (111) and (200) peaks. Note that the Cr_7C_3 peaks were matched with PDF #00- 036-1482

Planar SEM/EDS analysis was used to evaluate the microstructure and composition of the Ni-201 samples after corrosion tests. Figure 4 shows that the surfaces of the Ni-201 samples from both corrosion experiments are covered by a "web" structure. EDS Cr and Ni maps of both sample sets shows that this "web" structure is rich in Cr and deficient in Ni suggesting that a Cr-rich film deposited on the surface due to mass transport from 316L capsule. The nature of this Cr-rich film is unknown at present but could either be a Cr film or a chromium carbide film as suggested by the XRD patterns in Figure 3.

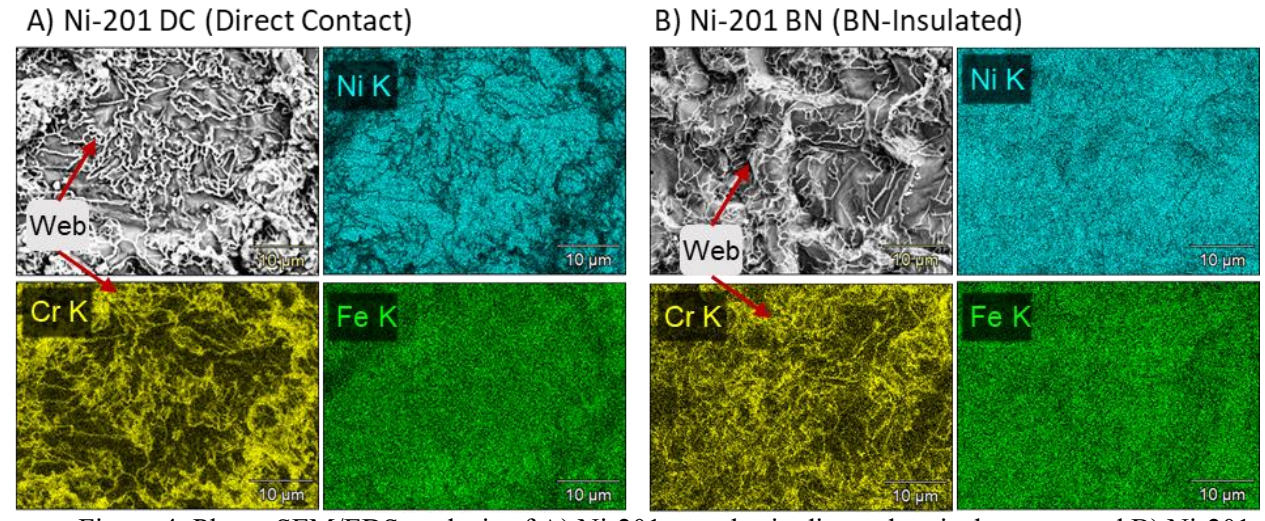


Figure 4: Planar SEM/EDS analysis of A) Ni-201 samples in direct electrical contact and B) Ni-201 samples BN-insulated from the 316L capsule.

SEM/EDS line scans and compositional maps were performed in the cross-sections of the Ni-201 samples. Figure 5 shows a cross section of the sample with direct electrical contact to the capsule. The EDS line scan, in Figure 5B, was collected along a grain boundary that approximately runs perpendicular to the sample surface in order to estimate the maximum diffusion of elements into the Ni-201. The Fe concentration at the sample surface is about 12 wt% and Fe diffusion into the Ni-201 sample extends to a depth of about 16 μm. The Cr compositional map in Figure 5F shows that there is a thin film of Cr on the sample surface that likely corresponds to the "web" structure observed in Figure 4A. The Cr EDS map and line scan indicate diffusion of Cr into the sample, although to a lesser extent than the Fe. The cross-sectional EDS analysis clearly shows that in the near-surface regions of the Ni-201 sample has a Ni-Fe-Cr ternary composition grading down to the original concentrations of Ni-201 alloy at greater depths. This result would

explain the peak separation observed in the XRD patterns shown earlier in Figure 3. The mixture of Ni-Fe-Cr introduces strain in an FCC lattice resulting in the slightly lower 2θ values for the (220), (311), and (222) peaks. At low 2θ values, the CuK- α x-rays have a lower penetration depth into the sample and only the (111) and (200) peak of the Ni-Fe-Cr FCC phase and a small shoulder of the Ni FCC phase are observed. However, at higher 2θ values the x-ray penetration depth is larger and the (220), (311), and (222) peaks in the Ni-201 bulk alloy show higher intensities.

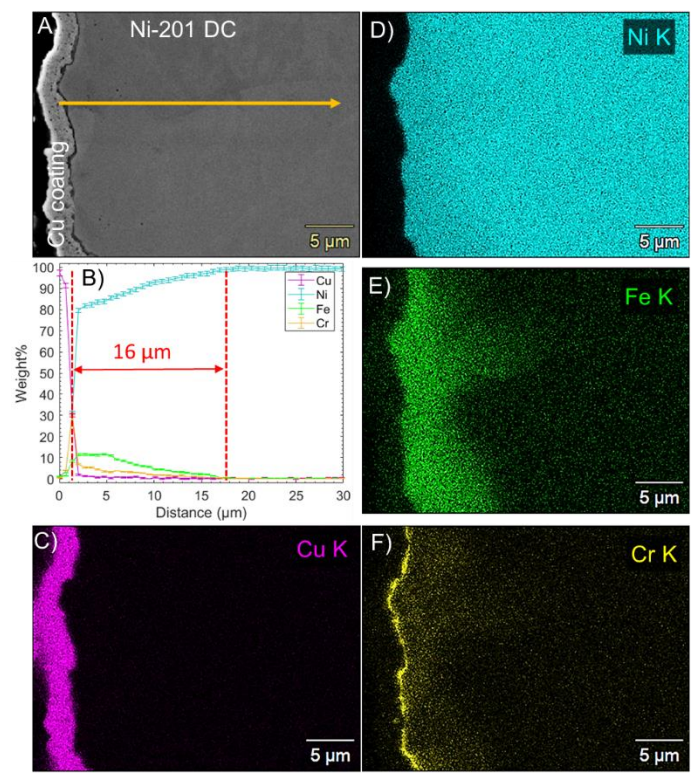


Figure 5: A) Cross-sectional SEM image of the Ni-201 sample from corrosion tests in which the samples and capsule were in direct electrical contact. B) EDS line scan collected along the yellow line shown in A). C-F) EDS maps for Cu, Ni, Fe, and Cr respectively. Note that the Cu was electroplated on the sample for edge retention.

The cross-sectional SEM/EDS of the Ni-201 sample from the insulated test is shown in Figure 6. The cross-sectional compositional profiles for Ni-201 from the two experiments were very similar, and this is consistent with the weight gain analysis for the two types of samples. A thin Cr rich layer at the sample surface can be observed in Figure 6F, which again likely corresponds to the "web" structure observed in Figure 4B. The EDS line scan shown in Figure 6B indicates that Fe (and to a lesser extent Cr) has diffused into the sample to a depth of about 19 µm and has a concentration of 14 wt% near the surface of the Ni-201

electrically isolated with BN. The depth of Fe diffusion is slightly higher for samples from the BN insulated corrosion tests, which may also explain the slightly higher weight gain for these samples.

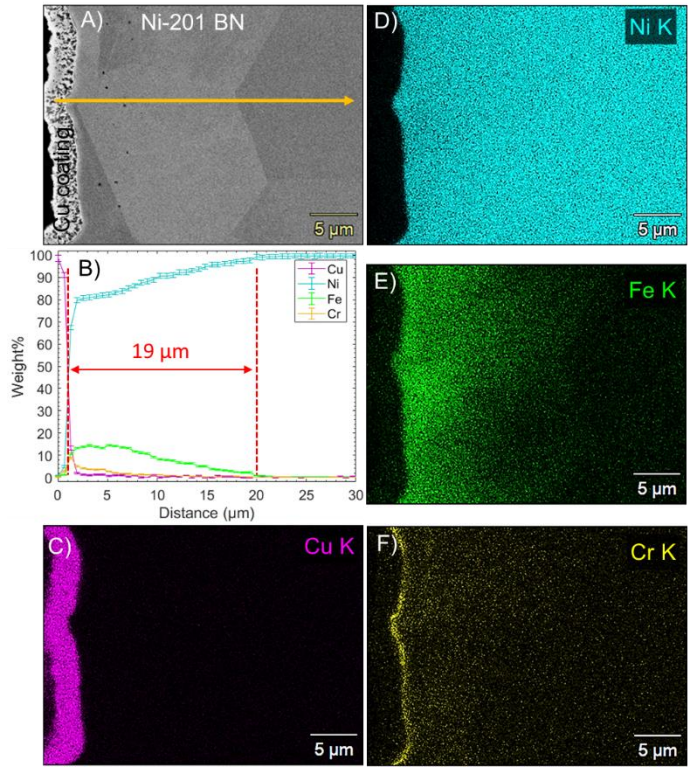


Figure 6: A) Cross-sectional SEM image of the Ni-201 samples after corrosion tests with BN electrical isolation. B) EDS line-scan data collected along the yellow arrow in A). C-F) EDS maps for Cu, Ni, Fe, and Cr respectively. Note that the Cu was electroplated on the sample for edge retention.

In order to get a better representation of the average Fe and Cr concentration profiles as a function of depth, GDOES was performed. GDOES sputters a 4 mm diameter circular region of material and uses an optical emission spectrometer to identify and quantify the elements being sputtered away. Since the quantification area is about 12.5 mm², the concentration profile collected by GDOES is a better representation of the average concentrations for Fe and Cr as a function of depth into the Ni-201 sample.

A comparison of the concentration versus depth profiles measured by EDS line scan and GDOES is shown in Figure 7. In Figure 7B and D, it can be seen that the GDOES concentration profiles for Ni, Fe, and Cr follow the same trends as the EDS line scans, again shown in Figure 7A and C. The diffusion depth of Fe measured by GDOES in both sample sets appears to be slightly less than the depths observed by EDS analysis at the grain boundary. The peak concentrations of Fe near the sample surface using the two

techniques appears to be similar. Using GDOES, it is also possible to detect carbon more reliably than with EDS and at a better spatial resolution. There is a peak in the Cr and C concentration at the sample surface, in Figure 7B and C. The peak concentrations of either Cr or C could not be quantitatively compared as the system was calibrated using samples that only varied from 0-25 wt% Cr and 0-2 wt% C and it appears the concentration of Cr and C at the sample surface is beyond the limits of the calibrated concentrations. However, qualitatively these results do support chromium carbide formation as suggested earlier by XRD analysis.

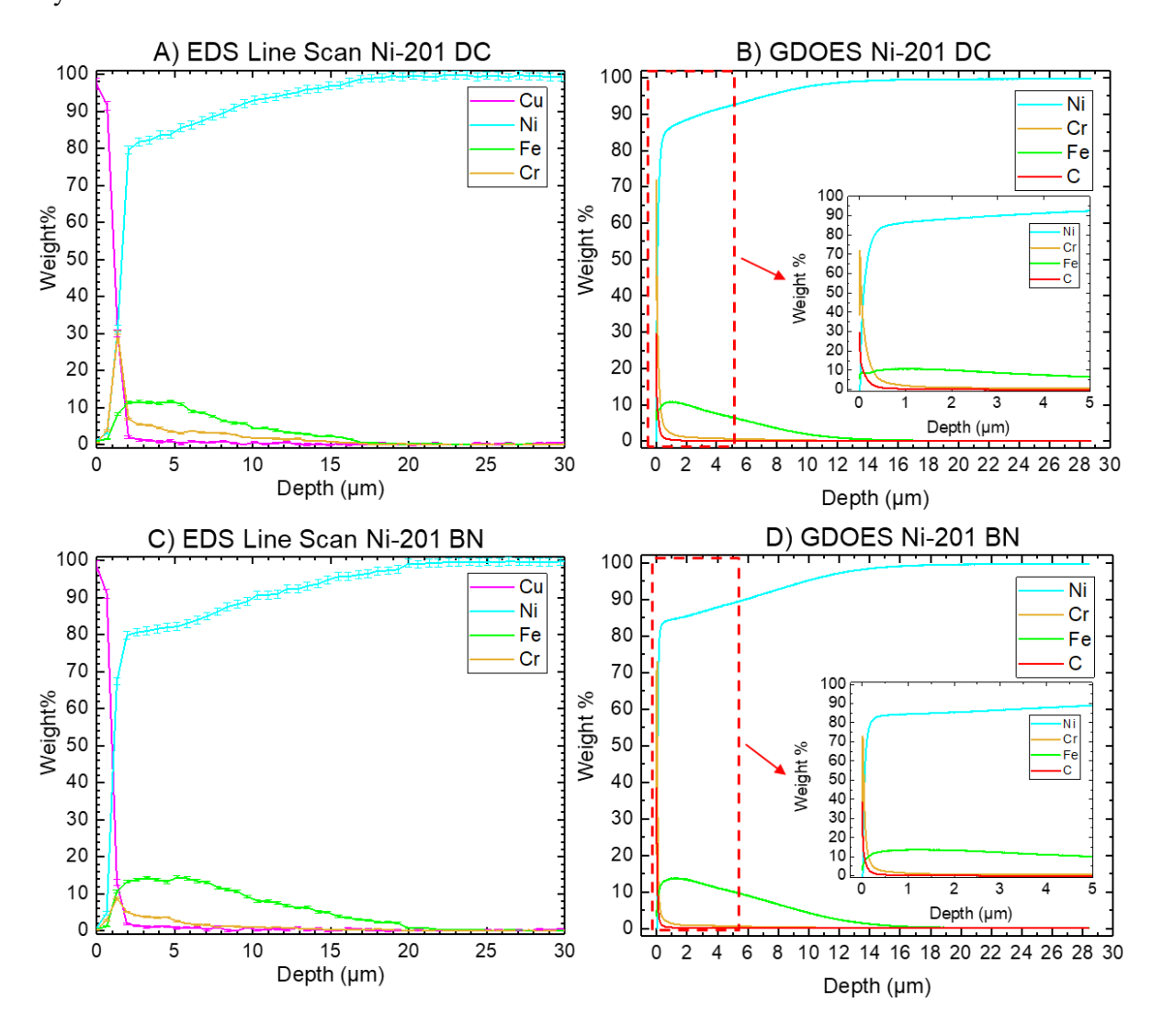


Figure 7: EDS line scan and GDOES profile comparison:(A) EDS line scan from Figure 5B, and (B) GDOES profile collected on Ni-201 samples in electrical contact with the capsule; (C) EDS line scan from Figure 6B, and (D) GDOES profile collected on Ni-201 samples which were electrically isolated from the capsule with BN. Note that the quantification of the GDOES was completed independently of the EDS results.

4 Discussion

The results of this study show that even when the samples and the capsule are electrically isolated from each other, corrosion products can migrate through the molten salt and deposit onto the surface of the more noble material. In this study, the corrosion products migrated from the 316L corrosion capsule to the Ni-201 samples resulting in weight gain whether or not the Ni-201 samples were electrically isolated from the 316L capsule. The average increase in mass was slightly higher for the samples from the corrosion tests in which the samples were electrically isolated with BN. However, this slight difference in average weight gain is not significant enough to suggest that a different mechanism may be at play in the two capsules. This result has important implications on corrosion of structural material when in use in molten salt environments because it confirms that corrosion in the presence of dissimilar materials can induce mass transport even if best efforts to electrically isolate materials is taken.

From the GDOES profiles shown in Figure 7B and D for the Ni-201 sample in direct electrical contact and the Ni-201 sample electrically isolated from the 316L capsule, an effective diffusion coefficient for both Fe and Cr into Ni-201 can be calculated by considering Fick's second law of diffusion, Eq. (2).

$$\frac{\partial C}{\partial t} = D_{eff} \frac{\partial^2 C}{\partial x^2}$$
 Eq. (2)

Determining the exact boundary conditions represents a challenge for two reasons. First, the diffusion coefficients of Fe and Cr in molten FLiNaK are unknown, such that the exact time that Fe and Cr have reached the Ni-201 surface is not defined. Second, the concentrations of both Cr and Fe at the surface of the Ni-201 samples change as a function of the exposure time. With respect to the first challenge, it can be reasonably assumed that the diffusion of Fe and Cr through the molten FLiNaK is orders of magnitude quicker than the diffusion of Fe and Cr in Ni-201, so that the total time of diffusion in Ni-201 can be assumed to be the total test time of 500 hours. Further simplification to reach a solution to Fick's second law was done by assuming that the actual value of the Fe and Cr concentration at Ni-201 sample surface is the maximum value of the Fe concentration in the GDOES profiles. It was then assumed that the concentration of both Fe and Cr at this location are a constant concentration source for both Fe and Cr.

Finally, the concentration of both Fe and Cr in the bulk of the Ni-201 samples remained at their nominal compositions in Ni-201 as reported in Table 2. With these assumptions, the solution to Fick's second law is:

$$C(x,t) = C_s - (C_s - C_o) \operatorname{erf}\left(\frac{x}{2\sqrt{D_{eff}t}}\right)$$
 Eq. (3)

This solution was then fitted to the concentration profiles of both Fe and Cr in the GDOES profiles to solve for the effective diffusion coefficient for both Fe and Cr in the Ni-201 sample in direct electrical contact and in the Ni-201 sample electrically isolated from the 316L capsule. The results from the fitting are reported in Table 4 alongside literature values for the diffusion coefficients of Fe and Cr in pure Ni. Further information on the fitting procedure can be found in the supplemental material. The effective diffusion coefficients are much higher compared to the the diffusion coefficients reported in literature for the solid-state diffusion of both Fe and Cr in pure Ni. This is likely explained by the fact that the effective diffusion coefficient found in this work is a combination of both solid state and grain boundary diffusion. Evidence of grain boundary diffusion is best seen in Figure 5E where the diffusion of Fe appears to be deepest along the grain boundary where the EDS line scan was taken.

Table 4: Diffusion coefficients determined from fitting Eq. (3) to GDOES data in Figure 7. Values of Fe and Cr diffusion coefficients from literature are also reported.

Source	$D_{Fe}^{Ni}(700^{o}C) (\text{cm}^{2}/\text{s})$	$D_{Cr}^{Ni}(700^{o}C) \text{ (cm}^{2}/\text{s)}$	Notes
Ni-201 DC (This work)	1.34×10^{-13}	4.57×10^{-14}	
Ni-201 BN (This work)	2.05×10^{-13}	1.37×10^{-13}	
Wu et al. [20]	1.54 x 10 ⁻¹⁵	2.5 x 10 ⁻¹⁵	Solid state diffusion coefficient calculated with DFT
Bakker et al. [21]	3.5×10^{-15}		Experimentally determined on pure Ni single crystals
Ruzickova et al. [22]		1.8 x 10 ⁻¹⁵	Experimentally determined by radiographic tracing

Mass transport mechanisms in molten salts without electrical contact have been proposed previously. Koger et. al. [23] observed migration of both cobalt and chromium from Haynes alloy No. 25 (53 wt% Co and 19 wt% Cr) to Hastelloy-N (0.1 wt% Co and 6.9 wt% Cr) in experiments in a fluoroborate salt loop.

Koger et. al. explained that the migration of chromium and cobalt from the Haynes alloy No. 25 was partially due to an activity gradient mass transfer. In this mechanism the chromium and cobalt have a relatively high activity in the Haynes alloy No. 25 and can reach lower activity levels by reacting chemically with the molten fluoroborate salt, diffusing through the salt, and depositing on the Hastelloy-N. Once deposited these elements diffused into the Hastelloy-N alloy [23].

Work by Ozeryanaya [13] and later work by Olson et al [24] also explained the non-galvanic mass transfer of elements in molten chloride and fluoride salts as driven by an activity gradient and that the transport of elements is enabled by oxidation and reduction through a disproportionation reaction that takes place on a metal surface, as seen in Figure 8.

$$3MF_{2(d)} = 2MF_{3(d)} + M_{(s)} \tag{1}$$

Here subscript s represents a solid and d indicates a dissolved fluoride compound. This disproportionation reaction leads to an atom being deposited, M_s , on the metal surface. The deposited atom can then form an intermetallic compound with, or diffuse via solid state mechanism into, the metal. Ozeryanaya and Olson suggested that this disproportionation reaction would only occur on an alloy surface, as described by Olson [24]. While the disproportion reaction could take place at a metal surface, it is likely that the reaction would also take place elsewhere in the corrosion capsule.

Williams et al. [19] report that, because FLiNaK is a fluorobasic salt, both Cr and Fe can form oxidation states of 2+ and 3+ in molten FLiNaK because the salt is likely totally dissociated. Due to the relatively low thermodynamic free energy of formation of their respective fluorides, it would be expected that both Cr and Fe are susceptible to dissolution via the following reactions at the surface of the 316L corrosion capsule, as shown in Figure 8:

$$M_{(316)} + F_{2(q)} \rightleftharpoons MF_{2(d)}$$
 (2)

$$M_{(316)} + \frac{3}{2} F_{2}_{(g)} \rightleftharpoons M F_{3(d)}$$
 (3)

where $M_{(316)}$ indicates either Fe or Cr in the 316L capsule. Olander [25] theorized that the activity of dissolved metal fluorides as shown in reaction (4), is controlled by the activity of dissolved fluorine described as the fluorine potential, $\Delta \overline{G_{F_2}}$, reaction (5).

$$\frac{a_{MF_n}}{a_M} = exp\left(\frac{\Delta \overline{G_{F_2}} - \Delta G_{MF_n}^o}{RT}\right) \tag{4}$$

$$\Delta \overline{G_{F_2}} = RT ln(a_{F_2}) \tag{5}$$

Where $\Delta G_{MF_n}^o$ is the free energy of formation of the chromium or iron fluorides, n is the number of fluoride (2 or 3), R is the gas constant, and T is the absolute temperature. Olander also suggests that the amount of dissolved fluoride in the salt can be controlled by adjusting the fluorine potential, and hence the activity of the dissolved fluoride, via (i) control of the gas phase, (ii) the introduction of a redox buffer, or (iii) electrochemical methods. In the present study, the experiment was conducted using FLiNaK prepared from high purity constituents and conducted in an inert atmosphere environment, but further control of the fluorine potential was not attempted. Thus, the fluorine potential was likely high enough in the starting salt to favor a high degree of dissolution of both Fe and Cr in the form of fluorides. Hence for Fe and Cr, reaction (2) and reaction (3) are likely product favored [26].

Upon the introduction of $MF_{2(d)}$ and $MF_{3(d)}$ into the salt a disproportionation reaction in the FLiNaK salt must occur, as shown in reaction (6) and illustrated in Figure 8.

$$3MF_{2(d)} \rightleftharpoons 2MF_{3(d)} + M_{(d)} \tag{6}$$

Where $M_{(d)}$ is now metallic Fe or Cr that is dissolved in FLiNaK. Dissolved Fe and Cr may migrate in the salt by convection or diffusion, driven by chemical potential gradients to the Ni-201 sample where it is possible for the dissolved metal to react with the Ni-201, as shown in Figure 8:

$$M_{(d)} \rightarrow M_{(Ni-201)} \tag{7}$$

here M_{Ni-201} represents Fe or Cr that is now a solute within the Ni-201 matrix. Considering the relatively high solubility of Fe and Cr into Ni, solid state diffusion of Fe and Cr into Ni-201 matrix is favored. Reaction (7) consumes $M_{(d)}$ and is perpetuated by the disproportionation reaction, reaction (6), which proceeds toward the products. Whether or not the disproportionation reaction is taking place at the Ni-201 surface as shown in reaction (1), or in the FLiNaK salt as shown in reaction (6), the Ni-201 sample can act as a sink for Fe and Cr. In the case of reaction (1), the diffusion of Fe and Cr into the Ni-201 removes $M_{(s)}$ product from the reaction. Reaction (6) presents a slightly more complicated situation. In this case, reaction (7) removes product from reaction (6) and diffusion removes $M_{(Ni-201)}$ product from reaction (7). Nevertheless, the continuous removal of reaction products through the Ni-201 sink, may imply that the original corrosion reactions of the 316L, reaction (2) and reaction (3), capsule may also never reach equilibrium and the Ni-201 may increase the corrosion rate of 316L.

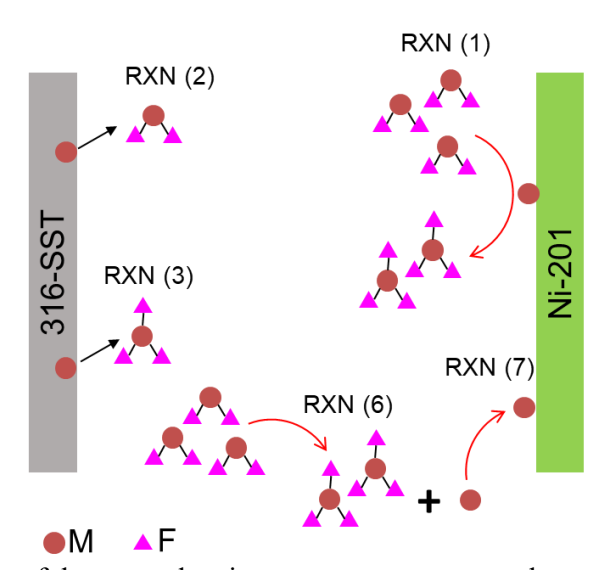


Figure 8: Schematic of the non-galvanic mass transport process between 316L and Ni-201.

The mechanism is also possible when one of the dissimilar materials is non-metallic, such as graphite. Olson et. al. exposed *electrically* connected Incoloy-800H samples in graphite crucibles to FLiNaK and found that Cr from the Incoloy-800H samples migrated to the graphite crucible and diffused into the graphite matrix [24]. Sellers et. al. [17] observed a similar effect for 316L and Hastelloy-N samples exposed to FLiNaK salt that contained a graphite coupon. A visibly silver colored chromium carbide coating was observed on the graphite after exposure. This mechanism for mass transport does not require electrical contact between the Ni-201 samples and the 316L corrosion capsule to maintain charge balance. The effect likely is dependent upon the solubility of one metal in the other or the ability of the metals to form an intermetallic compound. If neither metal prefers to form a solid solution or the two metals do not form an intermetallic with one another, the activity of one metal in the other is likely high and reaction (7) is less likely to occur. In this case, the equilibrium of the disproportionation reactions will be unaffected since corrosion product is not being removed.

5 Conclusion

Corrosion and mass transport effects from the presence of dissimilar materials (Ni-201 test samples and 316L stainless steel capsule) in molten FLiNaK salt after 500-hour exposure at 700 °C have been investigated. Two experiments were conducted, one in which the test capsule and samples were electrically connected and the other where they were electrically isolated from each other with a BN insulator. Characterization of the Ni-201 samples using SEM-EDS, XRD, and GDOES showed that in both cases corrosion products Fe and Cr from the 316L capsule were transported via the molten salt on to the Ni-201 sample. Due to the high temperatures of exposures in the corrosion test, both Fe and Cr diffused into the Ni-201 test sample in effect forming a Ni-Cr-Fe ternary alloy in the near surface regions of the Ni-201 samples. Fe diffused deeper into the test samples than Cr. A thin Cr-rich film was observed on the surface of Ni-201 samples while mild XRD peaks corresponding to Cr-carbide were also observed, possibly induced by carbon impurity in the salt from the preparation of the salt in a graphite crucible. ICP-MS analysis of the salt before and after corrosion showed a significant enhancement of Cr concentration in the

salt after the corrosion tests. In all these results, there was no significant difference between the experiments where the test samples and the capsule were electrically connected or electrically isolated from each other, suggesting that corrosion is exacerbated by dissimilar effects and mass transport is driven by activity gradients rather than galvanic effects.

The results and conclusions of this work strongly suggest that the choice of corrosion container and sample material are uniquely intertwined, and that the choice of materials could influence the observed corrosion rates in an unexpected way. For this reason, test samples and corrosion container materials should be carefully chosen to properly determine corrosion rate in a laboratory setup. In addition, this mass transport phenomenon absolutely needs to be taken into account in the materials selection for MSR designs.

CRediT Authorship Contribution Statement

Cody Falconer: Conceptualization, Methodology, Investigation, Writing - Original Draft. William Doniger: Methodology, Investigation, Writing - Review & Editing. Louis Bailly-Salins: Investigation, Writing - Review & Editing. Evan Buxton: Writing - Review & Editing. Mohamed Elbakhshwan: Investigation, Writing - Review & Editing Kumar Sridharan: Writing - Review & Editing, Supervision, Funding acquisition. Adrien Couet: Writing - Review & Editing, Supervision, Funding acquisition

Declaration of Competing Interest

The authors declare that they have no known competing financial interests or personal relationships that could have appeared to influence the work reported in this paper.

Acknowledgements

This work was partially funded under an IRP grant (Grant No. DE-NE0008651) from the United States Department of Energy, Office of Nuclear Energy, as well as NEUP grants (Grant No. DE-NE0008802 and DE-NE0008803) from the United States Department of Energy. Any opinions, finding, conclusions or recommendations expressed in this publication are those of the author(s) and do not necessarily reflect the views of the Department of Energy, Office of Nuclear Energy. The authors gratefully acknowledge use of

facilities and instrumentation at the UW-Madison Wisconsin Centers for Nanoscale Technology (went.wisc.edu) partially supported by the NSF through the University of Wisconsin Materials Research Science and Engineering Center (DMR-1720415). Special thanks to Martin Shafer and the Trace Element Research Group at the Wisconsin State Laboratory of Hygiene for collecting the ICP-MS data presented in this paper.

Data Availability

The raw/processed data required to reproduce these findings cannot be shared at this time as the data also forms part of an ongoing study.

References

- [1] M. Elbakhshwan, W. Doniger, C. Falconer, M. Moorehead, C. Parkin, C. Zhang, K. Sridharan, A. Couet, Corrosion and Thermal Stability of CrMnFeNi High Entropy Alloy in Molten FLiBe Salt, Scientific Reports, 9 (2019) 18993.
- [2] S.S. Raiman, S. Lee, Aggregation and data analysis of corrosion studies in molten chloride and fluoride salts, Journal of Nuclear Materials, 511 (2018) 523-535.
- [3] W.H. Doniger, K. Sridharan, Application of voltammetry for quantitative analysis of chromium in molten 2LiF-BeF2 (FLiBe) salt, Journal of Electroanalytical Chemistry, 838 (2019) 73-81.
- [4] D.A. Jones, Principles and Prevention of Corrosion, 2nd ed., Prentice-Hall, Inc., 1996.
- [5] L.C. Olson, J.W. Ambrosek, K. Sridharan, M.H. Anderson, T.R. Allen, Materials corrosion in molten LiF–NaF–KF salt, Journal of Fluorine Chemistry, 130 (2009) 67-73.
- [6] M. Kondo, T. Nagasaka, Q. Xu, T. Muroga, A. Sagara, N. Noda, D. Ninomiya, M. Nagura, A. Suzuki, T. Terai, N. Fujii, Corrosion characteristics of reduced activation ferritic steel, JLF-1 (8.92Cr–2W) in molten salts Flibe and Flinak, Fusion Engineering and Design, 84 (2009) 1081-1085.
- [7] X. Shi, K. Yu, L. Jiang, C. Li, Z. Li, X. Zhou, Microstructural characterization of Ni-201 weld cladding onto 304 stainless steel, Surface and Coatings Technology, 334 (2018) 19-28.
- [8] X.-X. Ye, H. Ai, Z. Guo, H. Huang, L. Jiang, J. Wang, Z. Li, X. Zhou, The high-temperature corrosion of Hastelloy N alloy (UNS N10003) in molten fluoride salts analysed by STXM, XAS, XRD, SEM, EPMA, TEM/EDS, Corrosion Science, 106 (2016) 249-259.
- [9] Q. Dai, X.-X. Ye, H. Ai, S. Chen, L. Jiang, J. Liang, K. Yu, B. Leng, Z. Li, X. Zhou, Corrosion of Incoloy 800H alloys with nickel cladding in FLiNaK salts at 850 °C, Corrosion Science, 133 (2018) 349-357
- [10] J. Hou, G. Yu, C. Zeng, H. Ai, R. Xie, Y. Chen, X. Zhou, L. Xie, J. Wang, Effects of exposing duration on corrosion performance in weld joint of Ni-Mo-Cr alloy in FLiNaK molten salt, Journal of Fluorine Chemistry, 191 (2016) 110-119.
- [11] Y. Zhu, J. Qiu, J. Hou, W. Liu, H. Chen, H. Ai, G. Yu, J. Wang, X. Zhou, Effects of SO42– ions on the corrosion of GH3535 weld joint in FLiNaK molten salt, Journal of Nuclear Materials, 492 (2017) 122-127.
- [12] W. Xue, X. Yang, Z. Li, X. Li, J. Wang, V. Ignatiev, X. Zhou, Effect of exposing duration on the interaction between nickel-based alloy and SiC in molten LiF-NaF-KF salt, Journal of Nuclear Materials, 515 (2019) 276-283.

- [13] I.N. Ozeryanaya, Corrosion of metals by molten salts in heat-treatment processes, Metal Science and Heat Treatment, 27 (1985) 184-188.
- [14] H. Ai, J. Hou, X.-X. Ye, C.L. Zeng, H. Sun, X. Li, G. Yu, X. Zhou, J.-Q. Wang, Influence of graphite-alloy interactions on corrosion of Ni-Mo-Cr alloy in molten fluorides, Journal of Nuclear Materials, 503 (2018) 116-123.
- [15] H. Sun, X. Ding, H. Ai, G. Lei, X. Yang, J.-Q. Wang, Interaction mechanisms of a Hastelloy N-316L stainless steel couple in molten LiF-NaF-KF salt, Corrosion Science, 164 (2020) 108317.
- [16] L. Olson, Materials Corrosion in Molten LiF-NaF-KF Eutectic Salt, in: Nuclear Engineering, University of Wisconsin Madison, 2009.
- [17] R.S. Sellers, W.-J. Cheng, B.C. Kelleher, M.H. Anderson, K. Sridharan, C.-J. Wang, T.R. Allen, Corrosion of 316L Stainless Steel Alloy and Hastelloy-N Superalloy in Molten Eutectic LiF-NaF-KF Salt and Interaction with Graphite, Nuclear Technology, 188 (2014) 192-199.
- [18] J. Qiu, B. Leng, H. Liu, D.D. Macdonald, A. Wu, Y. Jia, W. Xue, G. Yu, X. Zhou, Effect of SO42–on the corrosion of 316L stainless steel in molten FLiNaK salt, Corrosion Science, 144 (2018) 224-229.
- [19] D. Williams, L. Toth, K. Clarno, Assessment of Candidate Molten Salt Coolants for the Advanced High-Temperature Reactor (AHTR), in, Oak Ridge National Lab., 2006.
- [20] H. Wu, T. Mayeshiba, D. Morgan, High-throughput ab-initio dilute solute diffusion database, Scientific Data, 3 (2016) 160054.
- [21] H. Bakker, J. Backus, F. Waals, A Curvature in the Arrhenius Plot for the Diffusion of Iron in Single Crystals of Nickel in the Temperature Range from 1200 to 1400°C, physica status solidi (b), 45 (1971) 633-638.
- [22] J. Růžičková, B. Million, Self-diffusion of the components in the F.C.C. phase of binary solid solutions of the Fe Ni Cr system, Materials Science and Engineering, 50 (1981) 59-64.
- [23] J.W. Koger, A.P. Litman, Mass Transfer Between Hastelloy N and Haynes Alloy No. 25 in a Molten Sodium Fluoroborate Mixture, in, Oak Ridge National Laboratory, 1971.
- [24] L.C. Olson, R.E. Fuentes, M.J. Martinez-Rodriguez, J.W. Ambrosek, K. Sridharan, M.H. Anderson, B.L. Garcia-Diaz, J. Gray, T.R. Allen, Impact of Corrosion Test Container Material in Molten Fluorides, Journal of Solar Energy Engineering, 137 (2015) 061007-061007-061008.
- [25] D. Olander, Redox condition in molten fluoride salts: Definition and control, Journal of Nuclear Materials, 300 (2002) 270-272.
- [26] C.F. Baes, The Chemistry and Thermodynamics of Molten Salt Reactor Fuels, Nuclear Metallurgy, 15 (1969) 617-644.